ELECTROSEISMIC INVESTIGATION OF THE SHALLOW SUBSURFACE: FIELD MEASUREMENTS AND NUMERICAL MODELING

Oleg V. Mikhailov, Matthijs W. Haartsen, and M. Nafi Toksöz

Earth Resources Laboratory
Department of Earth, Atmospheric, and Planetary Sciences
Massachusetts Institute of Technology
Cambridge, MA 02139

ABSTRACT

Electroseismic phenomena in porous media, first observed almost 60 years ago (Ivanov, 1939), were recently "rediscovered" due to their potential to detect zones of high fluid mobility and fluid chemistry contrasts in the subsurface (Thompson and Gist, 1993; Haartsen *et al.*, 1995). However, a limited number of field studies of these phenomena reported in the literature were not able to support the results with an explicit comparison to theoretical predictions. In this paper, we demonstrate that electroseismic phenomena in porous media can be observed in the field, explained, and modeled numerically, yielding a good agreement between the field and the synthetic data.

We first outline the design of our field experiment and describe the procedure used to reduce noise in the electroseismic data. Then, we present and interpret the field data, demonstrating how and where different electroseismic signals originated in the subsurface. Finally, we model our field experiment numerically and demonstrate that the numerical results correctly simulate arrival times, polarity, and the amplitude-versus-offset behavior of the electroseismic signals measured in the field.

INTRODUCTION

A seismic wave propagating in a medium can induce an electrical field or cause radiation of an electromagnetic wave. These phenomena can be caused by a number of different physical mechanisms, but are collectively referred to as electroseismic. An overview by Parkhomenko (1971) describes piezoelectric and triboelectric effects, as well as streaming

currents, as the primary causes of electroseismic phenomena in rocks. In our study we focus on electroseismic phenomena in porous media generated by streaming currents.

In a fluid-saturated porous rock, adsorption of an electrical charge to the surface of solid grains creates an excess of mobile ions of the opposite sign in the pore fluid (Bockris and Reddy, 1970). When a seismic wave propagates in such a rock, it displaces the ion-carrying fluid with respect to the solid matrix, thus generating a streaming electrical current. The streaming current results in a macroscopic charge separation that induces an electrical field. The magnitude of this field depends on the electrochemical properties of the fluid-solid contact and the mobility of the pore fluid. Laboratory experiments (Parkhomenko and Tsze-San, 1964; Gaskarov and Parkhomenko, 1974; Parkhomenko *et al.*, 1975; Migunov and Kokorev, 1977; Mironov *et al.*, 1993) and theoretical studies (Frenkel, 1944; Neev and Yeatts, 1989; Pride, 1994) demonstrate that the magnitude of the induced electrical field depends on the type of pore fluid (air, water or hydrocarbons) and solid (siliciclastic or carbonate), as well as the mechanical properties and the structure of the medium (elastic moduli, porosity, permeability and saturation).

Our work investigates the electroseismic effects that occur when a seismic wave crosses or travels along an interface between two different porous media. The first effect studied in this paper is referred to as electroseismic conversion, and is shown in Figure 1. When a spherical P wave crosses an interface between two media, it creates a dipole charge separation due to the imbalance of the streaming currents induced by the seismic wave on opposite sides of the interface. The electrical dipole radiates an electromagnetic wave, which can be detected by remote antennas. This phenomenon was first detected in the experiments of Martner and Sparks (1959), and later in the experiments of Thompson and Gist (1993) and Butler *et al.* (1994). The electroseismic conversion at an interface between two materials was also measured in a laboratory experiment by Zhu *et al.* (1994). A theoretical model of the electroseismic conversion was recently developed by Haartsen and Pride (1994). Numerical simulations (Haartsen, 1995) demonstrated that electroseismic conversion can take place at permeability or fluid chemistry contrasts. Therefore, electroseismic conversion has the potential to become a geophysical tool capable of detecting zones of high permeability such as fractured zones, and interfaces such as an oil-water contact (Haartsen *et al.*, 1995).

The other electroseismic effect studied in this paper is an electrical field generated by a seismic head wave (Figure 2). When a seismic head wave travels along an interface between two media, it creates a charge separation across the interface which induces an electrical field. This electrical field moves along the interface with the head wave and can be detected by antennas when the head wave passes under them. This phenomenon was previously identified in the experiments of Neishtadt and Osipov (1959) and Martner and Sparks (1959). It was also present in the experiments of Butler *et al.* (1994), although the authors did not identify it.

Historically, studies of electroseismic phenomena in porous media were limited to laboratory or theoretical investigations, primarily due to the difficulty in recording ad-

equate signals in the field. There have been only a few reports of electroseismic field experiments published (Ivanov, 1939; Ivanov, 1940; Neishtadt and Osipov, 1959; Martner and Sparks, 1959; Zablocki and Keller, 1961; Broding *et al.*, 1963; Tome, 1975; Thompson and Gist, 1993; Butler *et al.*, 1994). Only a fraction of these reports explained the origin of the measured electroseismic signals (Neishtadt and Osipov, 1959; Martner and Sparks, 1959; Thompson and Gist, 1993; Butler *et al.*, 1994). None of these reports gave an explicit comparison of the field data with theoretical predictions.

The objective of our work is to demonstrate that electroseismic phenomena can be observed in the field, explained, and simulated numerically, yielding a good agreement between the field and synthetic data. In this paper, we first outline the design of our field experiment and describe the procedure used to reduce noise in electroseismic data. Next, we present and interpret the field data, demonstrating how and where different signals originated in the subsurface. In particular, we identify the electroseismic conversion and the head wave-generated electrical field. Finally, we model our field experiment numerically, and demonstrate that the numerical results correctly simulate the arrival times, polarities, and amplitude-versus-offset behavior of the electroseismic signals measured in the field.

FIELD DATA ACQUISITION AND NOISE REDUCTION PROCESSING

We conducted our field measurements at a site in Hamilton, Massachusetts. Figure 3 shows a diagram of the experimental layout and Figure 4 shows a generalized vertical cross-section of the subsurface at the site derived from a variety of previously collected geophysical data.

Field Experiments

During the field experiments, we recorded vertical ground motions and horizontal electrical fields generated by seismic waves propagating from a surface seismic source. The vertical ground motions were measured using an array of geophones. The horizontal electrical fields were measured with an array of dipole antennas. Each of the antennas consisted of a pair of grounded electrodes. A sledge hammer was used as the seismic source. For data recording, we used the DAS-1 data acquisition system manufactured by OYO Geospace Corporation. The system had a dynamic range of 132 dB and crosstalk between channels of less than -100 dB.

Trace A in Figure 5 is a typical example of an electrical signal recorded in the experiment. It is dominated by coherent signals of a nonelectroseismic nature which we will refer to as coherent noise. The major source of this coherent noise was electrical current induced in the ground by remote power lines. The other significant source of coherent noise was telluric current induced by the time variation of the Earth's magnetic field. In order to reduce the coherent noise induced by these currents, we stacked the data 100 times. To further reduce the coherent noise, we used the observation that the

telluric and power line-induced currents did not change phase throughout the survey area. Therefore, the noise generated by them was effectively the same close and far away from the seismic source. During data acquisition we recorded the coherent noise on two remote, mutually perpendicular antennas (see Figure 3), and as part of the data processing we subtracted it from the electrical records. It was necessary to use two mutually perpendicular antennas to record both horizontal components of the coherent noise because the telluric and the power line-induced currents changed direction and amplitude (but not phase!) with location due to variation of ground resistivity. The details of noise reduction in the electrical data will be described in a later section.

In our field work we encountered a number of undesirable effects that interfered with the electroseismic measurements. The most significant of these effects are listed below.

1. When metal rods were used as electrodes, a chemical reaction between the electrodes and the ground material generated significant electrode noise. Therefore, we used stable Ag-AgCl electrodes to minimize this effect.

2. When an aluminum or steel base plate was used, a high frequency electromagnetic pulse was generated at the moment of sledge hammer impact with the plate. To eliminate this pulse we used a nonmetallic (Lucite) block as a base plate.

3. When a long trigger cable lay on wet ground, the electrical current flowing through the cable at the moment of the hammer impact induced a current in the ground. This cable-induced current was detected by the antennas. In some of the experiments it obscured the electroseismic signals. In order to eliminate this current, we cut the trigger cable as short as possible and isolated it from the ground. In the future, we suggest the use of an optical trigger cable for electroseismic field work.

Noise Reduction in Electrical Data

Prior to the interpretation of the field data, it was necessary to remove the power line and telluric noise from the electrical records. Figure 5 shows the results of our noise reduction procedure. Trace A is an electrical signal recorded in the field. The signal-to-noise ratio in this trace is approximately 0.01. Trace F is the same trace after the noise was reduced and the signal-to-noise ratio was increased to about 10.0, i.e., by a factor of one thousand.

The first step in noise reduction was subtracting the coherent noise recorded on the remote antennas. We matched the coherent noise in each individual electrical trace with a linear combination of the two remote records of the noise. The coefficients of the linear combination were estimated to obtain the best match in the least–squares sense. After the coefficients were estimated, we subtracted the corresponding linear combination of the remote noise records from the electrical trace. In Figure 5, traces B and C are the remote noise records. Trace D is the result of subtraction of a combination of traces B and C from trace A, plotted to scale. Trace E is the same result magnified by a factor of one hundred. The signal-to-noise ratio in trace E is close to one. Therefore,

subtraction of the remote noise records increased the signal-to-noise ratio in trace E by approximately a factor of one hundred.

The coherent noise remaining in the electrical traces after the remote records subtraction was due mostly to power line induced currents. Fourier analysis showed that the traces contained up to 30 harmonics (frequency range of 60 Hz to 1800 Hz) of the fundamental power line frequency, which in our experiments varied from 60 Hz by about 0.1 Hz. The electroseismic signals recorded in our experiments had the same frequency content as the seismic waves that generated them. The main energy of the electroseismic signals was contained in the frequency interval from 10 Hz to 150 Hz. To eliminate the power line harmonics with frequencies much higher than the frequencies of the electroseismic signals, we used low-pass filtering in the Fourier domain. We set the cutoff frequency of the low-pass filter to be 600 Hz, in order not to smear the first breaks in the electrical traces. To eliminate the remaining 10 harmonics of the fundamental power line frequency we first estimated the frequencies, amplitudes and phases of these 10 harmonics by a least squares fit in the time domain (Butler and Russell, 1993), and then subtracted the corresponding sinusoids from the electrical traces. Trace F in Figure 5 is the result of subtracting the power line harmonics from trace E. The signal-to-noise ratio in trace F is 10.0. Thus, it is increased by a factor of ten compared to trace E.

As a result of applying the procedure described above, we reduced the coherent noise in the electrical records by a total factor of one thousand. The highest signal-to-noise ratio in the records presented in this paper is about 50 and the lowest is about 5.0.

INTERPRETATION OF ELECTROSEISMIC DATA

Figures 6–9 show the electroseismic data collected at the site. These figures show electrical signals recorded on 4 ft (1.2 m), 8 ft (2.4 m), 8 ft (2.4 m), and 16 ft (4.8 m) antennas, respectively. The spacing between the antennas in Figures 6 and 7 is 2 ft (0.6 m), and in Figures 8 and 9 it is 4 ft (1.2 m). The antennas measured the potential of the electrode closer to the source with respect to the electrode further away from the source. To interpret the field data, we identified various electroseismic signals, and determined their origin by correlating their arrival times and moveout velocity with the known velocity structure and positions of interfaces in the subsurface.

Our knowledge of the subsurface was derived from seismic refraction, resistivity and hydrogeological data available at the experiment site. Figure 4 shows a generalized vertical cross-section of the subsurface at the site. The top 2.5 ft (0.75 m) layer is organic soil. The P wave velocity of this layer increases gradually with depth, and on average is 650 ft/s (200 m/s). The resistivity of the soil is 2000 $\Omega \cdot m$. Below the top soil is an 8 ft (2.4 m) layer of unsaturated glacial till. The P wave velocity of the unsaturated till is 2400 ft/s (730 m/s) and the resistivity is 2000 $\Omega \cdot m$. The watertable is at a depth of 10.5 ft (3.2 m). Below the watertable is a 20 ft (6 m) layer of saturated glacial till with the P wave velocity of 4700 ft/s (1430 m/s) and the resistivity of 200

$\Omega \cdot m$. Below the saturated glacial till is bedrock which appears to be fractured granite with the P wave velocity of 12200 ft/s (3700m/s) and the resistivity of 5000 $\Omega \cdot m$.

In our field data we identified the electroseismic conversion of the incident P wave at the top soil–glacial till interface and the electrical field generated by the head wave traversing this interface. We also detected signals that can be associated with the electroseismic conversion of the incident P wave at the watertable and at the glacial till–bedrock interface.

Electroseismic Conversion at the Top Soil-Glacial Till Interface

The records in Figures 6–9 show a negative electrical pulse arriving simultaneously at the antennas between 3 ms and 4 ms (event A-A). The pulse can be seen in the first ten traces in Figures 6 and 7 and in the first five traces in Figures 8 and 9. The amplitude of the pulse is always the strongest at the antenna closest to the source, and decreases further away from the source. Based on the following analysis of the data we concluded that this pulse is the electroseismic conversion of the incident P wave at the interface between the top soil and the glacial till. First, the arrival time of this pulse appears to be the same at all the antennas. Therefore, it traveled with an electromagnetic wave velocity in the medium. Then, the amplitude of the pulse is the strongest close to the source, which suggests that the pulse originated directly below the source. And finally, since the pulse arrived approximately at the time the P wave generated by the source reached the interface between the top soil and the glacial till, we concluded that this pulse was due to the electromagnetic wave radiated from the interface at the time when the incident P wave crossed it.

Electrical Fields Generated by the Head Wave Traversing the Top Soil-Glacial Till Interface

Traces 6 through 12 in Figures 8 and 9 show an electrical pulse travelling along the antenna array with a finite moveout velocity (event B-B). This pulse consists of a positive (shaded) peak, a negative double trough, and another positive peak. The horizontal velocity of the pulse is equal to the P wave velocity of the unsaturated glacial till. The pulse arrives at the antennas about 2 ms prior to the arrival of the P wave refracted from the interface between the top soil and the glacial till. Therefore, this pulse is due to the electrical field generated by the seismic head wave traveling along the interface between the top soil and the glacial till.

Electroseismic Conversion at the Watertable and the Glacial Till-Bedrock Interface

In our electroseismic records, we identified signals which may be attributed to the electroseismic conversion of the incident P wave at the watertable and the glacial till–bedrock interface. Traces 5 through 11 in Figure 7 and traces 6 through 8 in Figure 6

show a negative pulse arriving at approximately 7 ms (event C-C). We estimated the vertical P wave traveltime to the watertable to be 7.5 ms. Consequently, this pulse can be attributed to the electroseismic conversion at the watertable. However, this pulse is largely obscured by the electroseismic conversion at the top soil-glacial till interface. Further experiments with a higher frequency source are necessary to separate this pulse from the electroseismic conversion at the top soil-glacial till interface to confirm its origin.

Traces 6 through 9 in Figure 8 show a negative pulse arriving at approximately 14 ms (event D-D). We estimated the vertical P wave traveltime to the glacial till-bedrock interface to be approximately 11.5 ms. Therefore, this pulse may be attributed to the electroseismic conversion at that interface. The same pulse can be observed in traces 6, 7, and 8 in Figure 9. However, the amplitude of this pulse is very small, and further experiments with a stronger source are necessary to determine the nature of this signal.

NUMERICAL SIMULATION OF ELECTROSEISMIC PHENOMENA

We chose to simulate the electroseismic conversion and the head wave induced electrical fields at the top soil-glacial till interface because these phenomena were most clearly identified in the field data. We based the simulation on the coupled acoustic and electromagnetic equations for a fluid-saturated porous medium (Pride, 1994). Below we summarize these equations and describe the model of the subsurface used in numerical simulation.

The acoustic wave propagation in the medium is assumed to be governed by the Biot equations for a fluid-saturated porous medium. In the frequency (ω) domain:

$$\nabla \cdot \underline{\underline{\tau}}_B = -\omega^2 \left[\rho_B \underline{u}_s + \rho_f \underline{w}\right]. \tag{1}$$

$$\underline{\underline{\tau}}_B = \left[K_G \nabla \cdot \underline{u}_s + C \nabla \cdot \underline{w}\right] \underline{\underline{I}} + G \left[\nabla \underline{u}_s + \nabla \underline{u}_s^T - \frac{2}{3} \nabla \cdot \underline{u}_s \underline{\underline{I}}\right] \tag{2}$$

$$-P = C \nabla \cdot \underline{u}_s + M \nabla \cdot \underline{w} \tag{3}$$

Here, $\underline{\underline{\tau}}_B$ is the bulk stress in the medium, P is the pressure in the pore fluid, $\underline{u}_s$ is the displacement in the solid, and $\underline{w}$ is the relative fluid-solid motion; ρ_B denotes the bulk density of the medium, and ρ_f denotes the fluid density; K_G, G, C, and M are the Biot moduli and incompressibilities of the medium (Biot, 1962; Pride *et al.*, 1992); and $\underline{\underline{I}}$ is the identity tensor.

The electromagnetic effects in the medium are described by the Maxwell equations:

$$\nabla \times \underline{E} = i\omega \underline{B} \tag{4}$$

$$\nabla \times \underline{H} = -i\omega \underline{D} + \underline{J} \tag{5}$$

$$\underline{D} = \epsilon_0 \left[\frac{\phi}{\alpha_\infty} (\kappa_f - \kappa_s) + \kappa_s \right] \underline{E} \tag{6}$$

$$\underline{B} = \mu_0 \underline{H} \tag{7}$$

where $\underline{J}$ is the electrical current density, $\underline{E}$ is the electric field strength, $\underline{D}$ is the electric displacement, $\underline{H}$ is the magnetic field strength, $\underline{B}$ is the magnetic induction, ϵ_0 is the permittivity of free space, μ_0 is the permeability of free space, κ_f is the relative permittivity in the fluid, and κ_s is the relative permittivity in the solid. ϕ is the porosity of the medium, and α_∞ is the tortuosity.

The coupling of acoustic and electromagnetic fields is assumed to be due to streaming electrical currents and electroosmosis. These effects are included into transport equations for the medium:

$$\underline{J} = \sigma(\omega)\underline{E} + L(\omega) \left[-\nabla P + \omega^2 \rho_f \underline{u}_s \right] \tag{8}$$

$$-i\omega \underline{w} = L(\omega)\underline{E} + \frac{k(\omega)}{\eta} \left[-\nabla P + \omega^2 \rho_f \underline{u}_s \right]. \tag{9}$$

Here, $\sigma(\omega)$ is the frequency-dependent electrical conductivity of the medium, $k(\omega)$ is the permeability, η is the fluid viscosity, and $L(\omega)$ is the electrokinetic coupling coefficient. The expressions for $\sigma(\omega)$, $k(\omega)$, and $L(\omega)$, as well as the detailed derivation of equations 1–9, are given in Pride (1995). Pride and Haartsen (1995) obtained eigenvector solutions for these equations in the frequency-wavenumber domain. Haartsen and Pride (1994) developed a numerical algorithm for solving boundary value problems in layered media by integrating over the eigenvector solutions. We used this algorithm for modeling the results of the field experiments.

To simulate the electroseismic effects at the interface between the top soil and the glacial till, we used a two-layer model. We assumed both layers to consist of an elastic porous frame with solid grains coated with water and the pore space saturated with air. The media parameters used for modeling are given in Table 2. We did not have information about the exact values of most of these parameters for the top soil and the glacial till at the site, and instead relied on the experimental data available for similar types of materials. We assumed 35 percent porosity for the top soil, and 15 percent porosity for the glacial till. The value of permeability assumed for the top soil corresponds to the values given by Geli *et al.* (1987) for loose sediments. The value of permeability assumed for the glacial till corresponds to the values given by Freeze and Cherry (1979) for moderately permeable sands and glacial tills. We further assumed that the top soil had 2 percent of water saturation and the glacial till had 20 percent of water saturation. We determined the effective density and permittivity of the air-water mixture based on their volumetric fraction in the pore space. To determine the effective viscosity, we assumed that the air-water flow in the pores is annular, and obtained the values of the effective viscosity for such flows from Wallis (1969). We also

assumed that the effective compressibility of the air-water mixture is determined by the compressibility of air.

Based on the above properties of the elastic frame and the pore fluid assumed for the top soil and the glacial till, we chose the frame moduli for both media such that the resulting P wave velocities matched the values measured in the field. The frame moduli chosen for the top soil and glacial till agreed with the values given by Geli *et al.* (1987) for loose sediments. We selected the values for salinity of water to yield media resistivity matching the values measured at the site, assuming that the conductivity of the medium was controlled by water coating the solid grains.

Based on the model described above, we calculated electrical and seismic fields generated by a vertical point source in an axisymmetric geometry. In order to allow for a sufficient separation of different electroseismic events, we used a Ricker wavelet with a 300 Hz center frequency as the source in our calculations.

COMPARISON OF FIELD AND SYNTHETIC DATA

Figures 10 and 11 show the seismic and electrical traces calculated, respectively. The seismic records in Figure 10 contain the waves reflected and refracted at the interface (direct and surface waves were not simulated). The electrical records in Figure 11 contain the signals due to electroseismic conversion of the incident P wave and the head wave-generated electrical field at the top soil-glacial till interface. The electrical records also contain signals generated by the other seismic waves.

The electrical traces in Figure 11 show a negative pulse arriving simultaneously on the antennas at approximately 3.8 ms (event A-A). This negative signal is the electroseismic conversion of the incident P wave at the interface between the top soil and the glacial till. The arrival time and the polarity of this pulse are the same as in our field measurements.

Figure 11 also shows a pulse consisting of a positive peak and a negative trough traveling along the antenna array with the P wave velocity of the glacial till (event B-B). A comparison with the seismic data in Figure 10 shows that this pulse arrives 2 ms earlier than the P wave refracted from the interface. Therefore, this pulse is due to the head wave-generated electrical field. The arrival times and the polarity of the pulse calculated numerically are consistent with the field measurements.

To compare the amplitudes of the electroseismic signals calculated numerically with those measured in the field, it was necessary to match the strength of the source used in the numerical calculation with the strength of the sledge hammer blow in the field. In order to achieve this, we compared the numerical and field amplitudes of the P wave refracted at the interface and scaled the numerical source strength so that these amplitudes agreed. We then used the same scaling for the electrical signals.

Figure 12 presents the amplitudes of the electroseismic conversion of the incident P wave at the interface, plotted in logarithmic coordinates versus the distance from the source. The amplitudes of the signals calculated numerically have a qualitatively

correct amplitude-versus-offset behavior. However, they are smaller than the observed amplitudes. Figure 13 presents the amplitudes of the electrical field generated by the head wave. Similar to the electroseismic conversion, the behavior of the amplitudes calculated numerically is qualitatively correct. However, their absolute values are smaller than the values measured in the field.

We therefore conclude that the numerical modeling correctly predicted the arrival times, polarity and qualitative amplitude-versus-offset behavior of the electroseismic conversion of the incident P wave at the top soil-glacial till interface and the electrical field generated by a head wave traversing this interface. It is also remarkable that despite the uncertainty of the lithology parameters and the modeling approximations, the numerical simulation was able to match the values of the amplitudes of the electroseismic signal within an order of magnitude.

CONCLUSIONS

We demonstrated that electroseismic phenomena can be observed in the field, explained, and simulated numerically, yielding a good agreement between the results of both field and numerical experiments.

We described the design of our field experiment and showed that it is possible to successfully eliminate noise and other undesirable effects to obtain clear electroseismic field records. In the field data we identified the electroseismic conversion of the incident P wave at the top soil-glacial till interface and the electrical field generated by the head wave traversing this interface. We also described signals that can be attributed to electroseismic conversion at the watertable and the glacial till-bedrock interface.

We numerically modeled the electroseismic conversion at the top soil-glacial till interface and the electrical field generated by the head wave traversing this interface. The numerical modeling correctly simulated the arrival times, polarities, and qualitative amplitude-versus-offset behavior of these electroseismic signals.

ACKNOWLEDGMENTS

This work was supported by the Department of Energy, Grant #DE-FG02-93ER14322 and by the Borehole Acoustics and Logging Consortium at the Massachusetts Institute of Technology. We thank Prof. Ted Madden, Dr. Randy Mackie, and Dr. Roger Turpening for helpful discussions regarding the design of the field experiment, electroseismic data processing and interpretation of the results. We are also grateful to Dr. Richard Gibson and Lt. Scott Carter (USAF) for their help in data acquisition. We thank Mr. Peter Britton of Hamilton, MA for his support of our research by making the site available for the experiments.

REFERENCES

Biot, M., 1962, Mechanics of deformation and acoustic propagation in porous media, *J. Applied Phys., 33*, 1482–1498.

Bockris, J., and Reddy, A. K. N., 1970, *Modern Electrochemistry,* Plenum Press.

Broding, R. A., Buchanan, S. D., and Hearn, D. P., 1963, Field experiments on the electroseismic effect, *IEEE Trans. Geosci. Electronics, GE-1*, 23–31.

Butler, K. E., and Russell, R. D., 1993, Subtraction of powerline harmonics from geophysical records, *Geophysics, 58*, 989–903.

Butler, K. E., Russell, R. D., Kepic, A. W., and Maxwell, M., 1994, Mapping of a stratigraphic boundary by its seismoelectric response, 1994 SAGEEP Annual Meeting, Proceedings, 689–699.

Freeze, R., and Cherry, J., 1979, *Groundwater,* Prentice-Hall,Englewood Cliffs.

Frenkel, J., 1944, On the theory of seismic and seismoelectric phenomena in a moist soil, *J. Physics (Soviet), 8*, 230–241.

Gaskarov, I. V., and Parkhomenko, E. I., 1974, The seismoelectric effect in rocks and the preconditions for its application in geological prospecting work, *Izv. Acad. Sci. USSR, Physics of the Solid Earth, 1*, 110–115.

Geli, L., Bard, P.-Y., and Schmidt, D. P., 1987, Seismic wave propagation in a very permeable water-saturated surface layer, *J. Geophys. Res., 92*, 7931–7944.

Haartsen, M. W., and Pride, S. R., 1994, Modeling of coupled electroseismic wave propagation from point sources in layered media, 64th Ann. Internat. Mtg., Soc. Expl. Geophys., Expanded Abstracts, 1155–1158.

Haartsen, M. W., Zhu, Z., and Toksöz, M. N., 1995, Electroseismic method for mapping the oil-water interfaces, presented at the Dharam, Saudi Arabia, June 11–13, 1995, Soc. Petr. Engineers.

Haartsen, M. W., 1995, Coupled electromagnetic and acoustic wavefield modeling in poro-elastic media and its applications in geophysical exploration, Ph.D. thesis, Massachusetts Institute of Technology.

Ivanov, A. G., 1939, Effect of electrization of earth layers by elastic waves passing through them (in Russian), *Doklady Akademii Nauk SSSR, 24*, 41–43.

Ivanov, A. G., 1940, The electroseismic effect of the second kind, *Izvestiya Akademii Nauk SSSR, Ser. Geogr. Geofiz.,* pp. 699–727.

Martner, S. T., and Sparks, N. R., 1959, The electroseismic effect, *Geophysics, 24*, 297–308.

Migunov, N. I., and Kokorev, A. A., 1977, Dynamic properties of the seismoelectric effect of water-saturated rocks, *Izv. Acad. Sci. USSR, Physics of the Solid Earth, 13*, 443–446.

Mironov, S. A., Parkhomenko, E. I., and Chernyak, G. Y., 1993, Seismoelectric effects of rocks saturated with gas or liquid hydrocarbons, *Izv. Acad. Sci. USSR, Physics of the Solid Earth, 11*, 70–76.

Neev, J., and Yeatts, F. R., 1989, Electrokinetic effects in fluid-saturated poroelastic media, *Phys. Rev. B, 40*, 9135–9141.

Neishtadt, N. M., and Osipov, L. N., 1959, Experimental studies of the electroseismic e-effect (in Russian), *Trans. VITR, 12*, 57–75.

Parkhomenko, E. I., and Tsze-San, C., 1964, A study of the influence of moisture on the magnitude of the seismoelectric effect in sedimentary rocks by a laboratory method, *Izv. Akad. Nauk SSSR, Geophys. Ser., 2*, 206–212.

Parkhomenko, E. I., Gaskarov, I. V., and Marmorshteyn, L. M., 1975, Relationship between the magnitude of the seismoelectric effect in sandstones and their permeability, *Dokl. Akad. Nauk SSSR, 223*, 1110–1111.

Parkhomenko, E. I., 1971, *Electrification Phenomena in Rocks,* Plenum Press, New York.

Pride, S. R., and Haartsen, M. W., 1995, Electroseismic wave properties (submitted), *J. Acoust. Soc. Am.*

Pride, R. S., Gangi, A. F., and Morgan, F. D., 1992, Deriving the equations of motion for porous isotropic media, *J. Acoust. Soc. Am., 92*, 3278–3290.

Pride, S. R., 1994, Governing equations for the coupled electromagnetics and acoustics of porous media, *Phys. Rev. B, 50*, 15678–15696.

Thompson, A. H., and Gist, G. A., 1993, Geophysical applications of electrokinetic conversion, *The Leading Edge, 12*, 1169–1173.

Tome, R. F., 1975, Studies on the seismoelectric effect, Master's thesis, University of Toronto.

Wallis, G. B., 1969, *One-Dimensional Two-Phase Flows,* McGraw-Hill Book Company.

Zablocki, C. J., and Keller, G. V., 1961, Some observations of the seismic-electric effect, U.S. Geolog. Survey Profess. Paper, Paper 424-D, D296–D299.

Zhu, Z., Cheng, C., and Toksöz, M. N., 1994, Electroseismic conversion in a fluid saturated porous rock sample, 64th Ann. Internat. Mtg., Soc. Expl. Geophys., Expanded Abstracts, 26–29.

Property	Top Soil	Glacial Till
porosity $\phi, [\%]$	35	15
dc permeability $k, [m^2]$	10^{-10}	10^{-12}
bulk modulus of the solid $k_s, [Pa]$	2.0×10^9	1.0×10^{10}
bulk modulus of the fluid $k_f, [Pa]$	1.4×10^5	1.4×10^5
bulk modulus of the frame $k_{fr}, [Pa]$	4.0×10^7	6.0×10^8
shear modulus of the frame $g_{fr}, [Pa]$	2.0×10^7	4.5×10^8
viscosity of the fluid $\eta, [Pa \cdot s]$	8.0×10^{-5}	6.0×10^{-4}
density of the solid $\rho_s, [Kg/m^3]$	2.2×10^3	2.4×10^3
density of the fluid $\rho_f, [Kg/m^3]$	20.0	200.0
salinity of the fluid $C, [mol/l]$	5.5×10^{-4}	1.2×10^{-3}
temperature $T, [K]$	298	298
permittivity of the solid κ_s	4	4
permittivity of the fluid κ_f	2.5	16
tortuosity α_∞	3	3

Table 1: The mechanical and electrical medium properties used for numerical modeling.

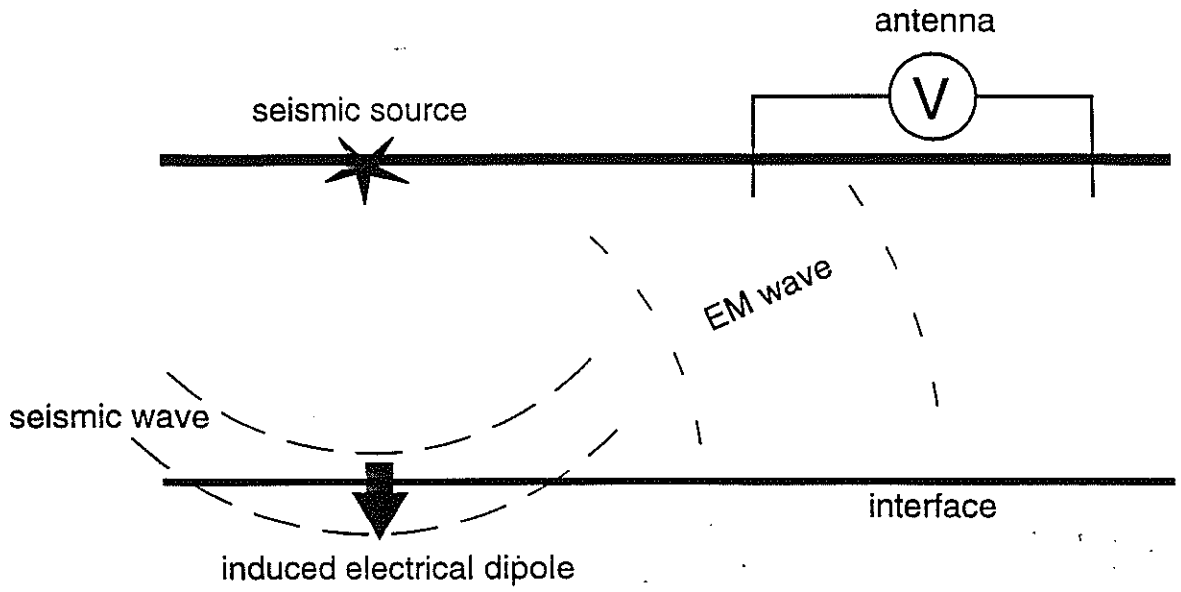

Figure 1: Diagram of the electroseismic conversion at an interface. When a spherical seismic wave crosses an interface, it creates a dipole charge separation across the interface. This electrical dipole radiates an electromagnetic wave which can be detected by remote antennas.

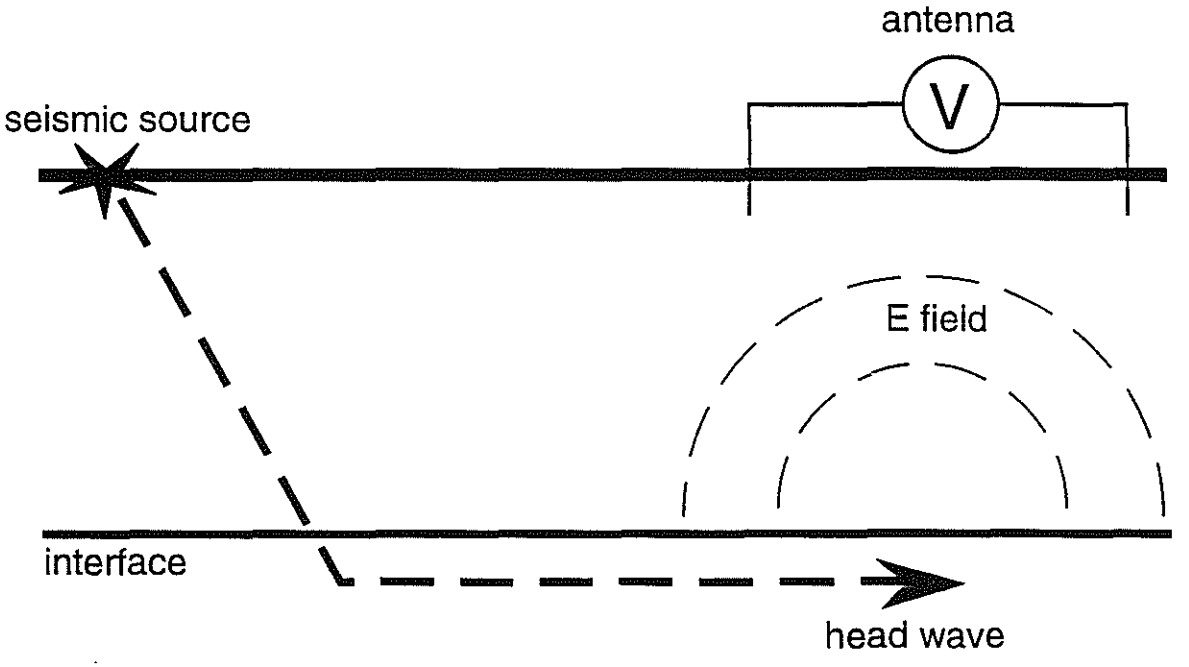

Figure 2: Diagram of the generation of an electrical field by a head wave traversing an interface. When a seismic head wave travels along an interface, it creates a charge separation across the interface which induces an electrical field. This electrical field can be detected by an antenna when the head wave travels below it.

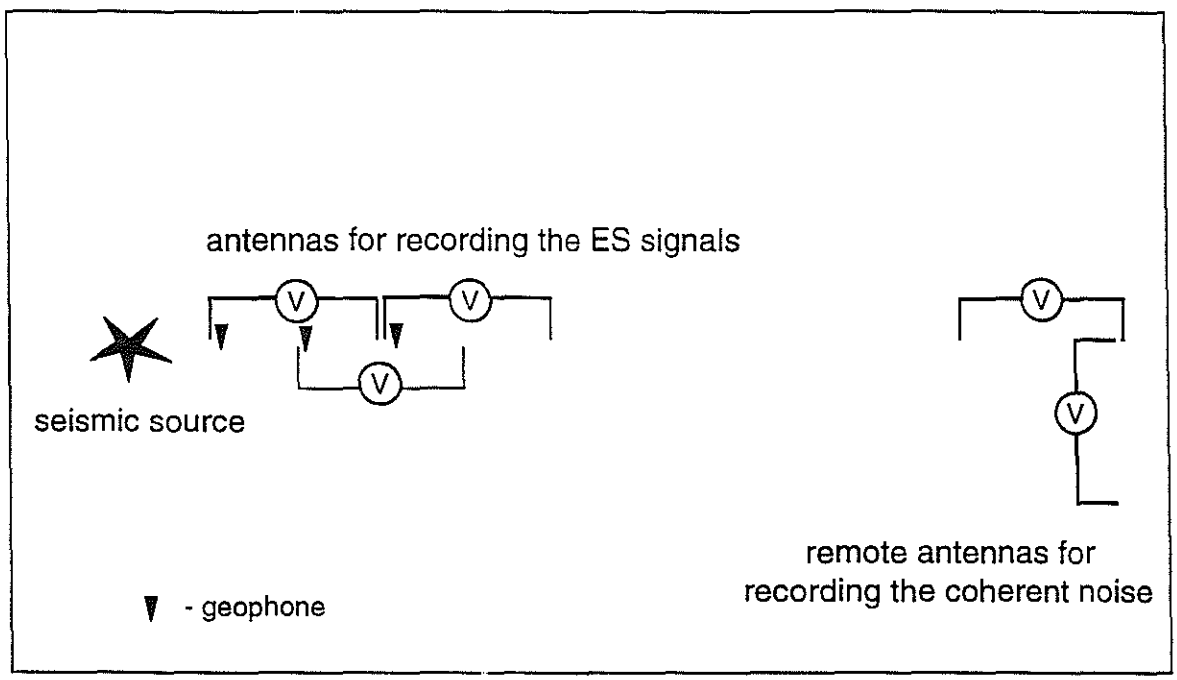

Figure 3: Diagram of the experimental layout (top view). In different experiments we used antenna lengths of 4 ft (1.2 m), 8 ft (2.4 m) and 16 ft (4.8 m). The offset between the source and antennas (measured to the electrode closest to the source) ranged from 2 ft (0.6 m) to 48 ft (14.6 m). The remote antennas were placed approximately 70 ft (21 m) away from the seismic source.

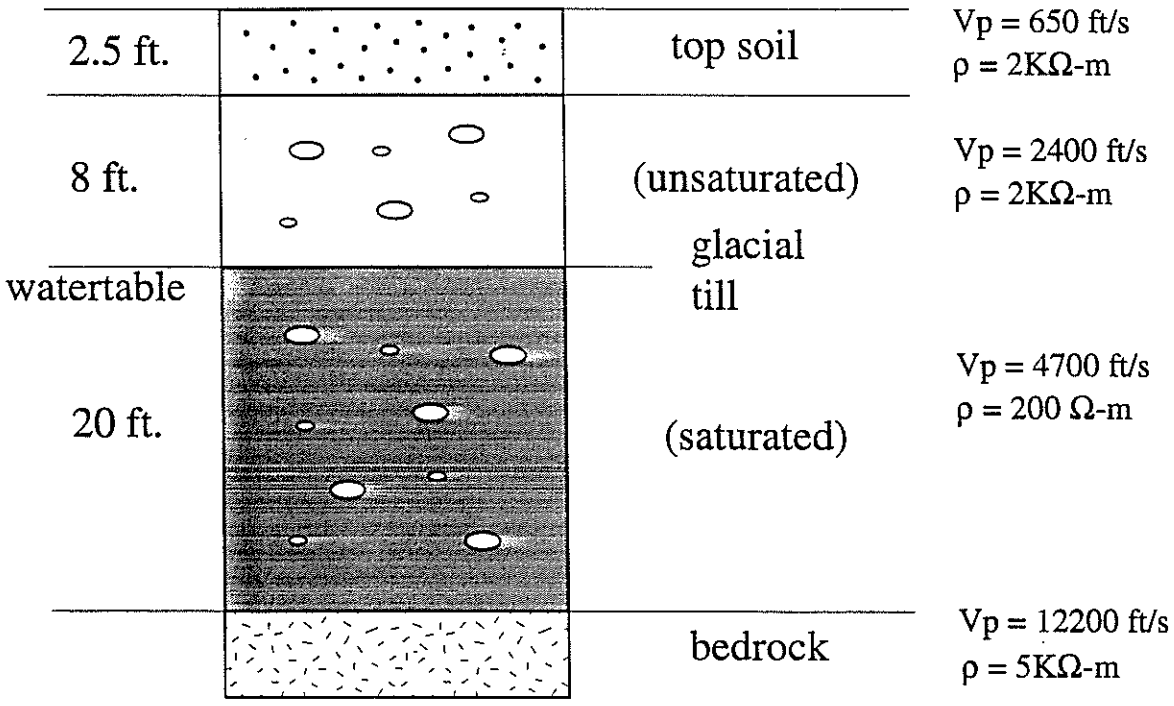

Figure 4: Generalized vertical cross-section (not to scale) of the subsurface at the experimental site derived from seismic refraction, resistivity and hydrogeological data.

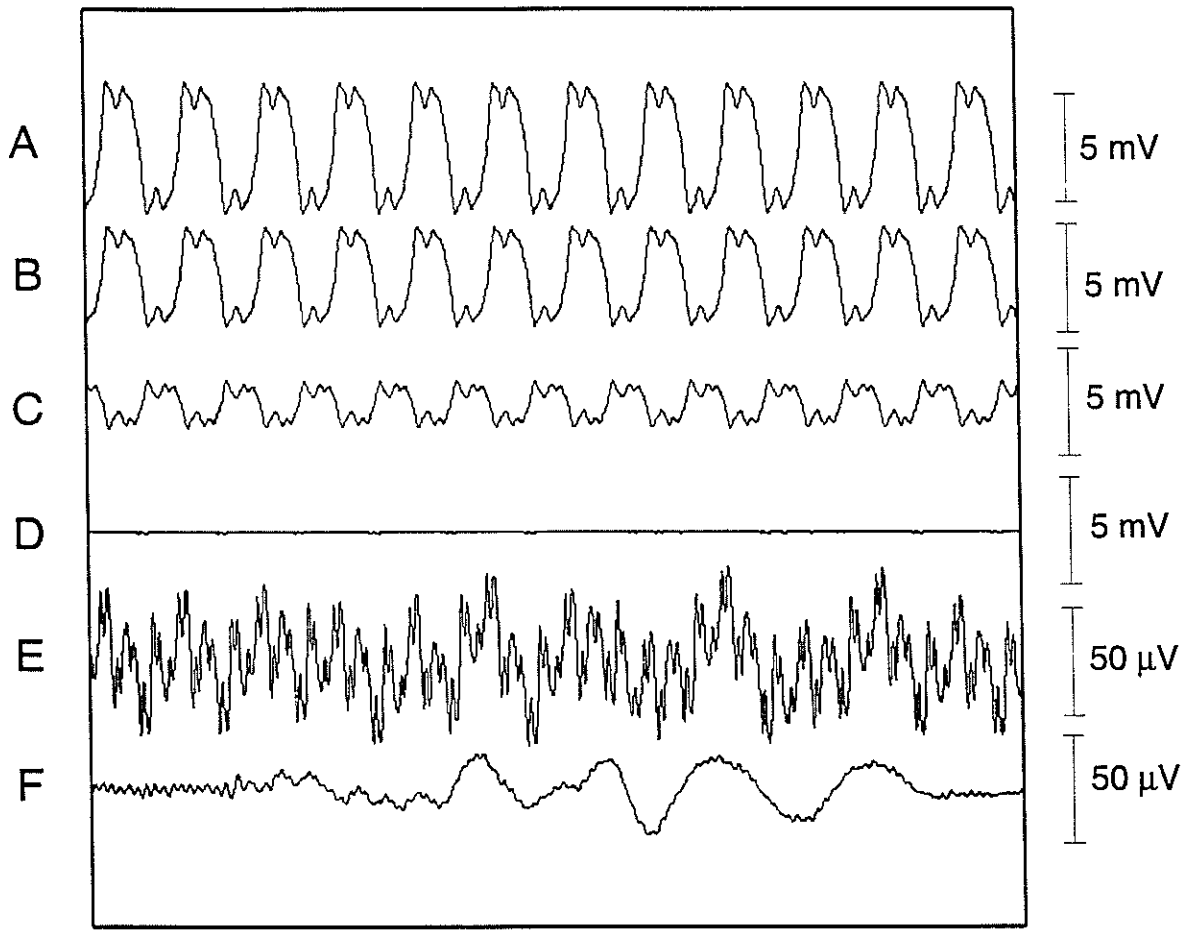

Figure 5: Noise reduction in the electrical data. Trace A is an electrical signal recorded in the field. The signal-to-noise ratio in trace A is about 0.01. Traces B and C are the remote noise records. Trace D is the result of subtracting a linear combination of traces B and C from trace A. Trace E is the same result magnified by a factor of one hundred. Trace F is the result of power line harmonics subtraction from trace E. The signal-to-noise ratio in trace F is about 10.0.

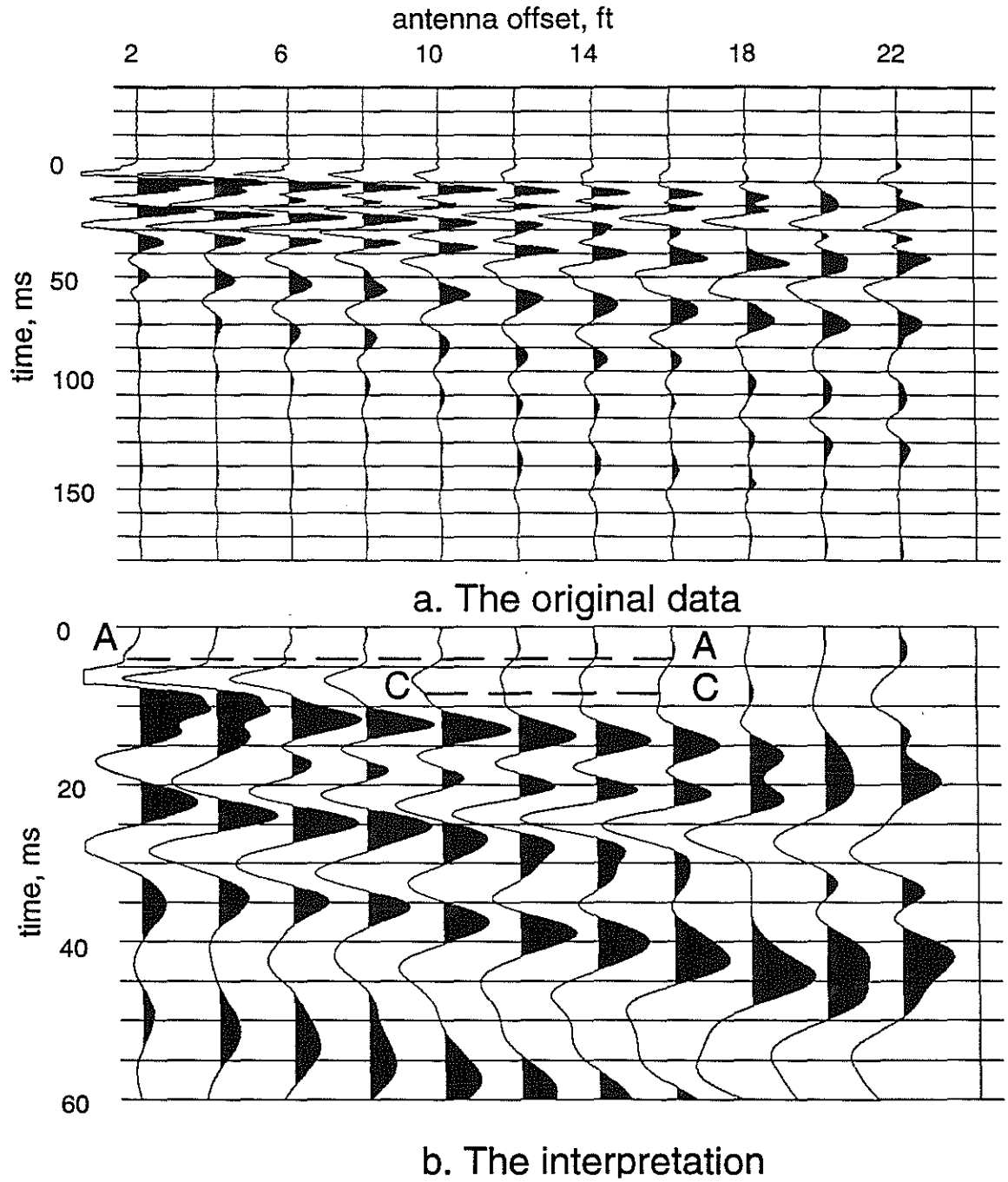

Figure 6: a) Electroseismic data collected at the site with 4 ft (1.2 m) antennas and 2 ft (0.6 m) spacing between the antennas. b) The first 60 ms of these data. Event A-A is the electroseismic conversion at the top soil-glacial till interface. Event C-C is possibly the electroseismic conversion at the watertable. Dashed lines mark the onset of these signals.

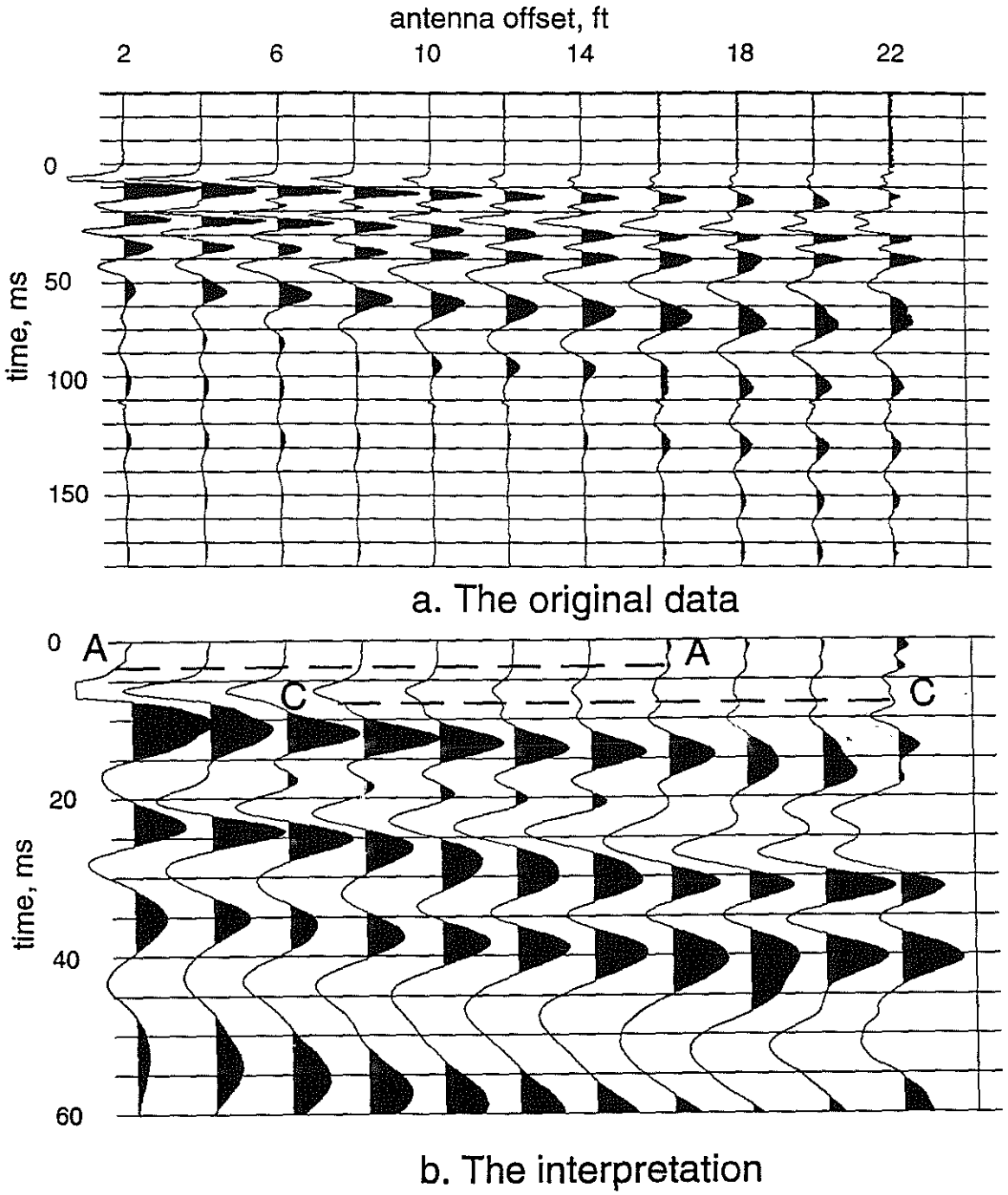

Figure 7: a) Electroseismic data collected at the site with 8 ft (2.4 m) antennas and 2 ft (0.6 m) spacing between the antennas. b) The first 60 ms of these data. Event A-A is the electroseismic conversion at the top soil-glacial till interface. Event C-C is possibly the electroseismic conversion at the watertable.

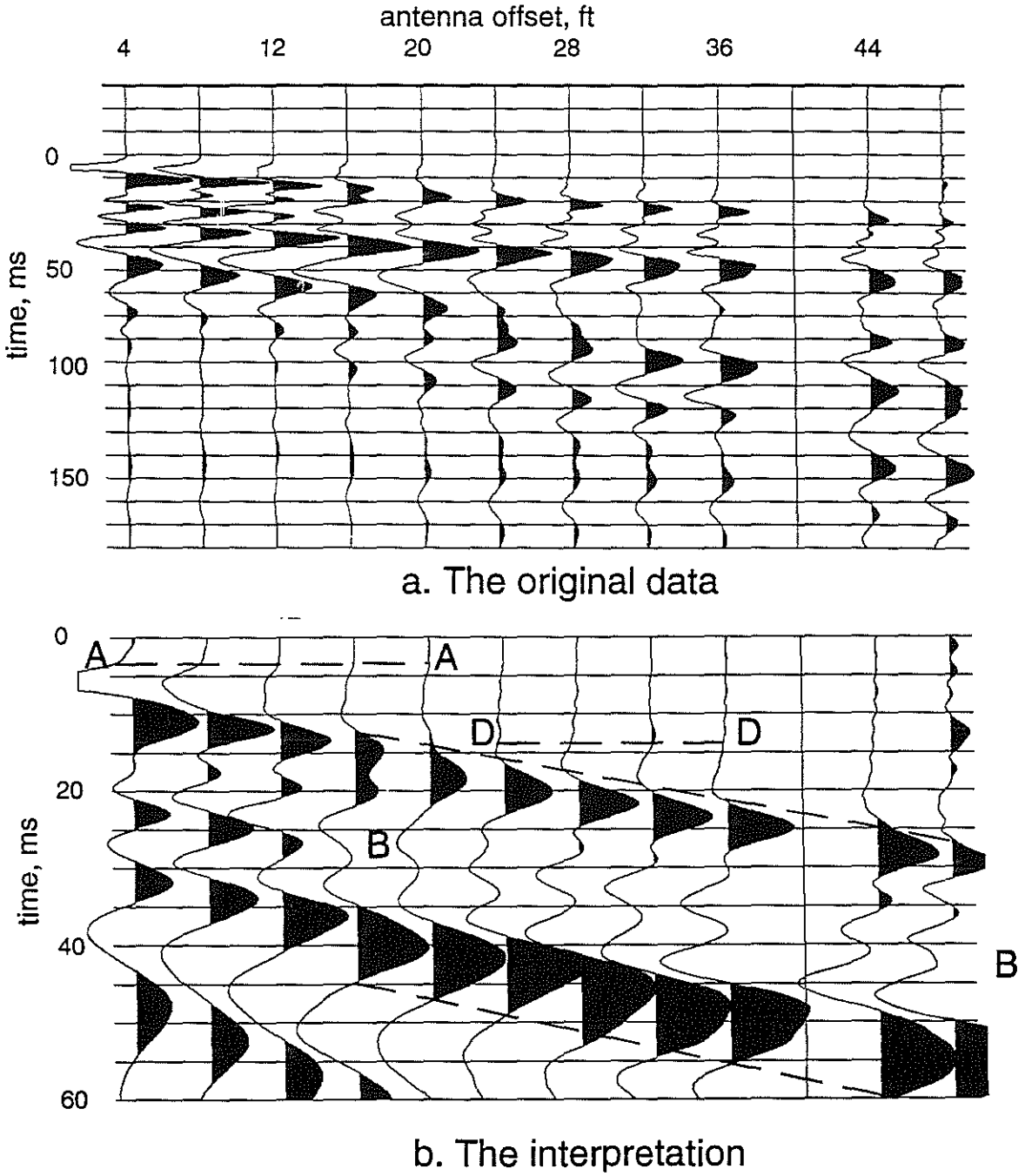

Figure 8: a) Electroseismic data collected at the site with 8 ft (2.4 m) antennas and 4 ft (1.2 m) spacing between the antennas. b) The first 60 ms of these data. Event A-A is the electroseismic conversion at the top soil-glacial till interface. Event B-B is the electrical field generated by the head wave traversing the same interface. Event D-D is possibly the electroseismic conversion at the glacial till-bedrock interface.

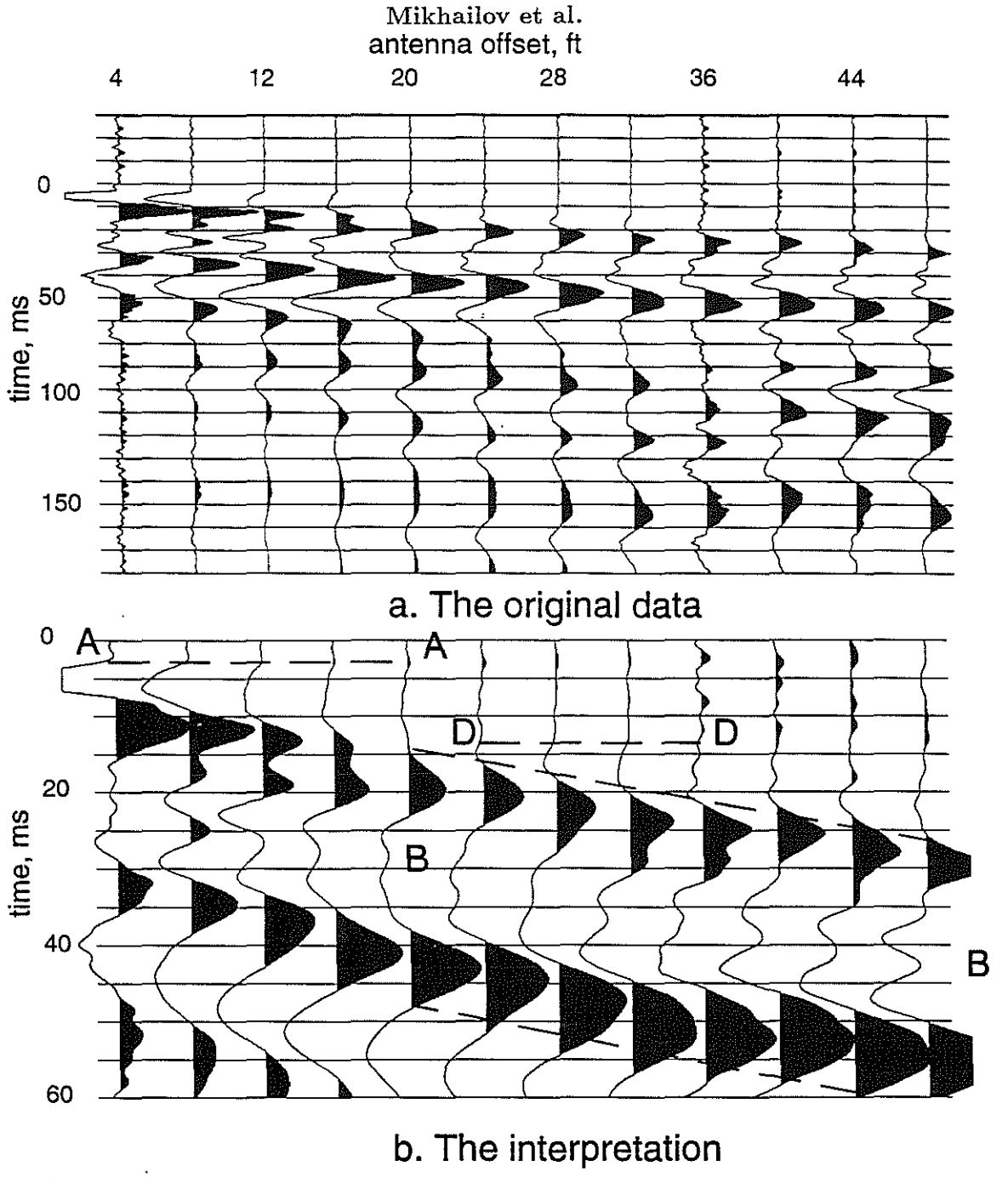

Figure 9: a) Electroseismic data collected at the site with 16 ft (4.8 m) antennas and 4 ft (1.2 m) spacing between the antennas. b) The first 60 ms of these data. Event A-A is the electroseismic conversion at the top soil-glacial till interface. Event B-B is the electrical field generated by the head wave traversing the same interface. Event D-D is possibly the electroseismic conversion at the glacial till-bedrock interface.

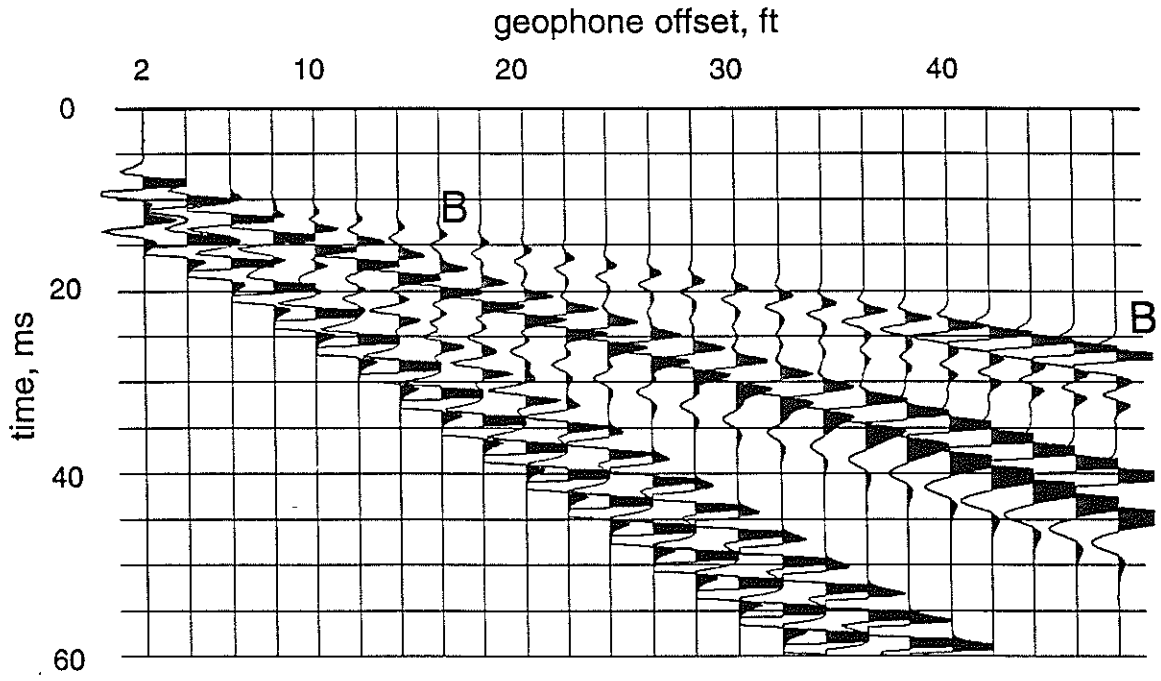

Figure 10: Synthetic seismic data. Event B-B is the refracted P wave. Two later events are the refracted S wave and the reflected P wave.

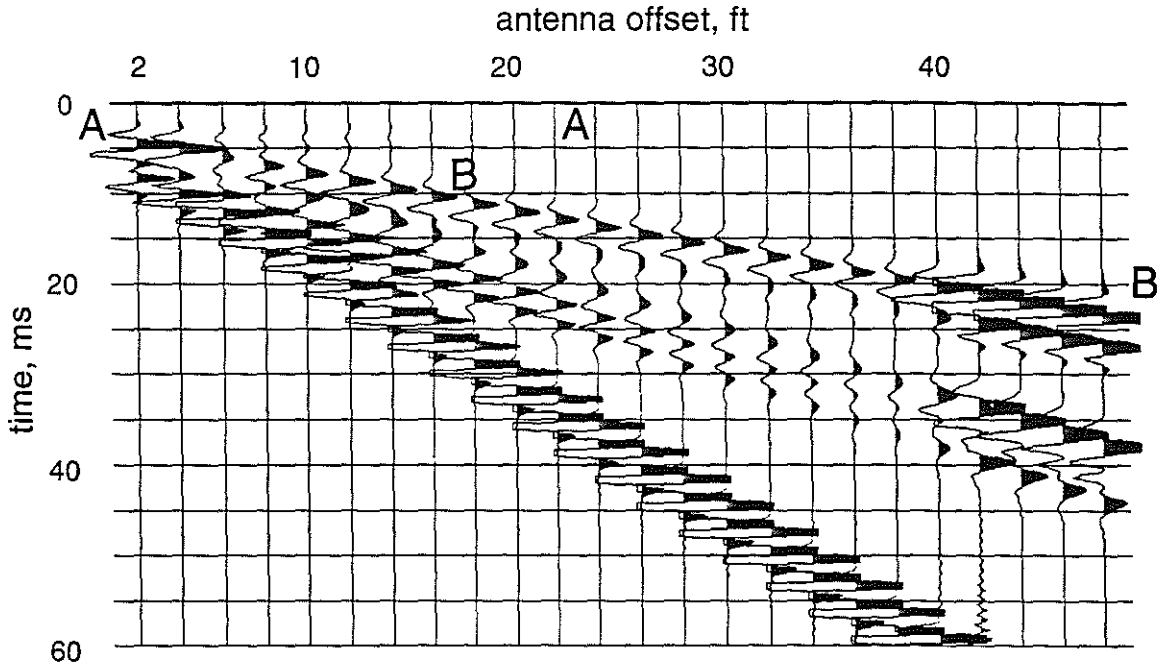

Figure 11: Synthetic electrical data. Event A-A is the electroseismic conversion at the interface. Event B-B is the electrical field generated by the head wave traveling along the interface. Two later events are due to electrical fields generated by the refracted S wave and the reflected P wave. In numerical calculations we used a noncausal Ricker wavelet. Therefore, we consider the time of a center peak as an arrival time, and the polarity of the center peak as the polarity of an electroseismic signal.

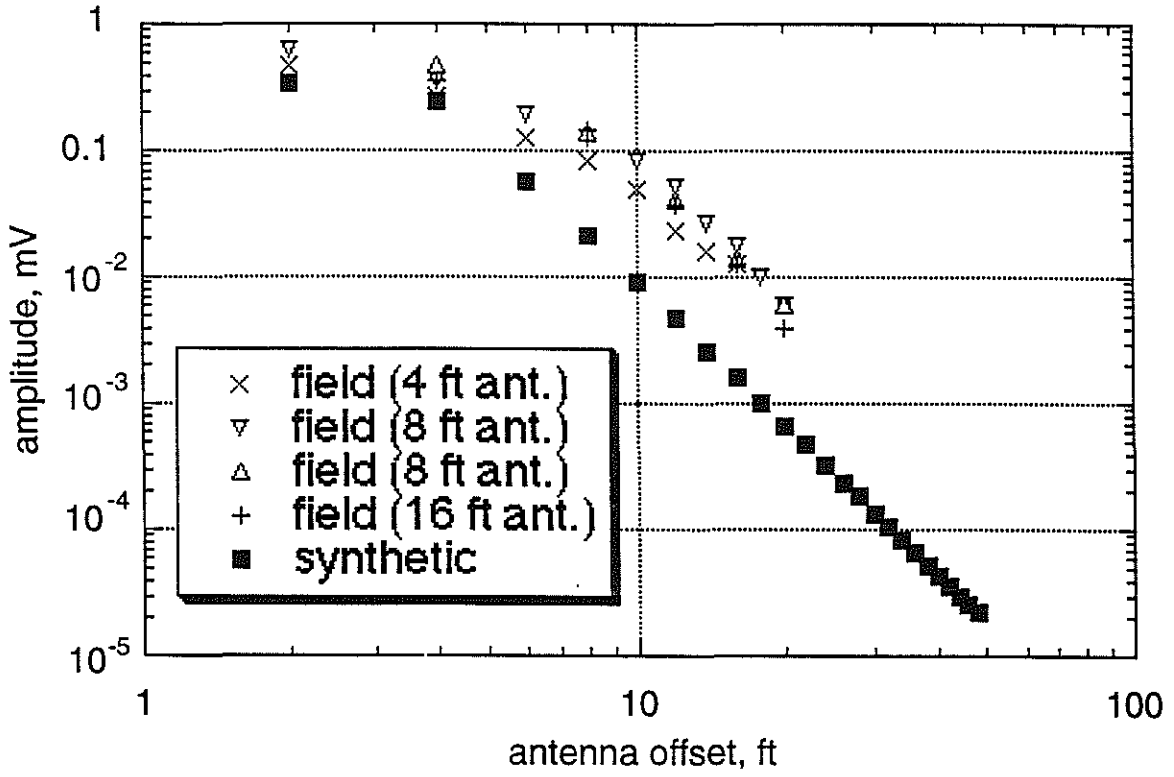

Figure 12: Comparison between the observed and the calculated amplitudes of the electroseismic conversion of the incident P wave at the top soil-glacial till interface.

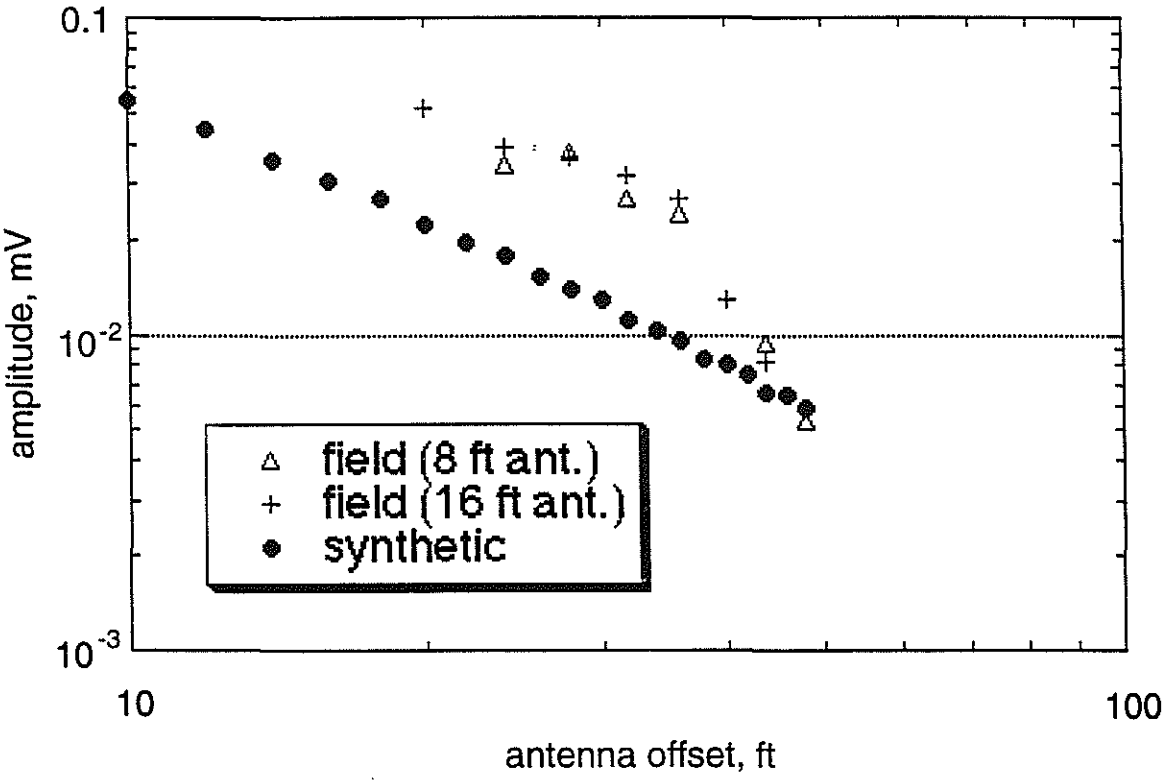

Figure 13: Comparison between the observed and the calculated amplitudes of the electrical field generated by the head wave traveling along the top soil-glacial till interface.